Axisymmetric and three-dimensional instabilities in an Ekman boundary layer flow

Eric Serre, Sandrine Hugues, Emilia Crespo Del Arco, Anthony Randriamampianina, Patrick Bontoux

Axisymmetric and three-dimensional instabilities in an Ekman boundary layer flow

E. Serre [a], S. Hugues [a], E. Crespo del Arco [b], A. Randriamampianina [a], P. Bontoux [a,*]

[a] *IRPHE, UMR 6594 CNRS, LABM, UMSR 2164, Université d'Aix-Marseille II, Dpt. Modélisation Numerique, La Jetée-IMT Château-Gombert, 38 rue Frédéric Joliot-Curie, 13451 Marseille cedex 20, France*

[b] *UNED, Departamento Fisica Fundamental, Apdo. 60.141, 28080 Madrid, Spain*

The instability of Ekman boundary layer flow is studied inside a rotating annular cavity with radial throughflow, which is a relevant geometry of the air cooling system in turbines. The flow is computed by direct numerical simulation using a time-dependent three-dimensional Navier–Stokes solver based on a pseudo-spectral method. The fluid entering the annulus at the inner section then develops into a rotating geostrophic core flanked above and below by two nonlinear Ekman boundary layers and exits at the outer section. In this study, the rotation rate of the cavity is fixed at a given high value, corresponding to an Ekman number $E = 2.24 \times 10^{-3}$. When the throughflow is weak, the motion is steady and the boundary layer flow is well described by Ekman's analytical solution. On increasing the mass flow rate, the flow becomes unsteady and perturbations appear in the form of counter-rotating pairs of vortices adjacent to upper and lower surfaces of the cavity. Multiple stable solutions, involving circular and spiral waves with different numbers of arms, are obtained at fixed mass flow rate. The wavenumber and frequency of both circular and spiral waves are determined to be characteristic of the type II viscous Ekman layer instability.

1. Introduction

The investigation of rotating viscous flows near walls has been the topic of many experimental, theoretical and numerical studies, motivated both by a fundamental geophysical interest (see Hide, 1968; Greenspan, 1969) and by applications to technological devices and their improvement (see Owen and Rogers, 1989, 1995). These applications have motivated studies in simple generic geometries and confined configurations that model actual complex situations. They concern a wide range of flows driven by the differential rotation of the walls, by radial throughflow, and also by heat transfer from the walls. Whereas the three-dimensional flow in an enclosed rotor–stator configuration has been recently studied by Serre et al. (1999a,b), the present investigation considers a cavity (of internal radius, a, and external radius, b) in which both disks are rotating at the same speed and there is superposed a radially outward throughflow. This configuration is highly confined by walls on two sides and the two remaining ones are the entrance and exit sections of the forced flow. This situation significantly models certain flows inside the rotating cavity of gas turbine engines. Although a large number of their features are also relevant to geophysical flows in the earth's atmosphere, the problem is entirely governed by engineering purposes. In air-cooled gas turbine engines, the cooling air is extracted from the HP compressor stages and is carried along a channel in order to cool the nozzle guide vanes, the turbine blades and the turbine disks to which the blades are attached. In certain types of engines, the air may be injected radially between two corotating compressor disks. A characteristic of these flows is the coexistence of adjacent coupled flow regions that are radically different in terms of the flow properties and of the length scales, as is the case for Ekman layers neighboring a geostrophic core region.

The first contributions to the field were theoretical and concerned the steady laminar flow of an incompressible viscous fluid driven by an infinite rotating disk studied by Von Karman (1921), who determined approximate analytical solutions that exhibited a thin boundary layer phenomenon. The length scale of this thin layer was clearly related to the rotation rate by Cochran (1934). The extension to confinement of isothermal laminar flow by two rotating disks has been studied analytically by Hide (1968) and Barcilon and Pedlosky (1967), and numerically by Chew (1984). The laminar flow structure in this configuration, involving a source mass flux at the entrance section, can be divided into four zones: an inner source region, two separated Ekman layers, an outer sink layer, and an interior inviscid core (Owen and Pincombe, 1980; Owen et al., 1985). Hide (1968) gave asymptotic solutions for the velocity distribution in the four regions by matching the linear Ekman

* Corresponding author. Tel.: +33-491-11-85-27/35; fax: +33-491-11-85-02.

layer solutions to the boundary layer solutions for the source and the sink. He also gave estimates for the radial extent of the source region and of the sink layer. The axisymmetric solution is composed of a geostrophic core and two Ekman layers on the upper and lower walls; the flow strength in the geostrophic core is related to the radial mass flux through the cavity, and the boundary layers are given by a well-known analytical solution (see, for example, Greenspan, 1969). The numerical studies of source–sink flows in a rotating annulus by Bennetts and Jackson (1974) confirm that the basic steady flow is well approximated by the analytical solution of Hide (1968), when the mass flow rate C_w is small, but as the flow rate increases, the linear solution becomes increasingly less accurate.

Various studies have delineated two generic forms of instability that develop in Ekman layers adjacent to rotating disks and that play an important role in the transition mechanism. They are referred to as either type II and type I instabilities or, respectively, type A and type B instabilities. The type I instability is associated with the presence of unstable inflection points in the velocity profiles normal to the disk plane, whereas Lilly (1966) showed with a linear stability analysis that the type II instability, appearing at lower values of the critical Reynolds number and with a larger wavelength, is related to the combined effects of the Coriolis forces and viscosity. This Reynolds number is usually defined as $Re = v_g^* \delta / \nu$, where v_g^* is the dimensional geostrophic azimuthal velocity, ν the kinematic viscosity of the fluid, and $\delta = (\nu/\Omega)^{1/2}$ is the characteristic boundary layer thickness in which Ω is the rotation rate of the plate. The waves associated with these types I and II instabilities are intrinsically different. Empirical relationships for the critical parameters were given by Tatro and Mollö-Christensen (1967) in the case of a radial inflow over the rotating plate, but one of these relations concerning the type I instability has been criticized by Cesaroli (1975) who suggested that these waves were only the result of disturbances induced by the measurement probe. The relations between the critical parameters for type II waves are approximately $(Re_c)^{II} = 56.3 + 58.4Ro$ and, for type I instability $(Re_c)^{I} = 124.5 + 3.66Ro$, with the Rossby number Ro defined as $Ro = v_g^*/(\Omega r^*)$, where r^* is the distance from the axis of rotation. Both instabilities have the form of either annular or spiral vortices located in the Ekman boundary layer. However, the types I and II vortices propagate in opposite directions and, consequently, the angle between the geostrophic velocity and the phase velocity of these waves have opposite sign; that angle lies between 0° and −20° for the type I waves and between 10° and 15° for the type II waves. These instabilities have been observed in the source–sink configurations by Faller (1963), Caldwell and Van Atta (1970) and in other kinds of rotating flows involving a Bödewadt layer by Savas (1987) and Wilkinson and Malik (1987), and more recently by Gauthier et al. (1999) and Schouveiler et al. (1999), and also in von Kármán boundary layer flows by Faller (1991) and Lingwood (1996). In Serre et al. (1999b), we report numerical investigations of the types I and II instabilities in an enclosed rotor–stator system, where annular and three-dimensional spiral patterns are found near the rotating and stationary walls.

In previous numerical investigations of flows involving Ekman boundary-layer instabilities, as in Marlatt and Biringen (1995), the curvature of the flow field was generally assumed to be negligible. However, this condition is satisfied only locally at large radii, where the stability analysis of Lilly (1966) is valid. The Rossby number Ro characterizes the effect of the nonlinear terms, which arise through the effect of the curvature. In the limit $Ro \to 0$, the wavelength of the vortices is independent of the radius and the wave front is a straight line normal to the flow. In Crespo del Arco et al. (1996), a pseudo-spectral numerical method was used to obtain axisymmetric unsteady solutions that arise in an annular configuration chosen to mimic the experiments of Owen et al. (1985), which models situations of practical interest. Thus, the curvature effects were included and oscillatory flow regimes were computed. These arise in the rotating cavity when the radial throughflow at the inlet is different to the Ekman layer solution. In the numerical simulations, at short distances from the axis, the inner velocity profile was chosen as a parabolic Poiseuille type profile in which case an entrance region develops which limits the radial displacement of the vortices. In such situations, Crespo del Arco et al. (1996) reported a transition to an oscillatory and a nonperiodic regime via a complex bifurcation scenario. In the unstable flow, six pairs of counter-rotating circular vortices, propagating radially outward, are found in the Ekman boundary layers. Their wavelength of about $24\sqrt{\nu/\Omega}$ and the frequency of about 7.4Ω are in good agreement with experimental results for similar values of Re and Ro as given by Caldwell and Van Atta (1970) and Weidman (1976). Experimental results with a smaller radii of curvature have shown circular waves and also types I and II spiral waves, Weidman (1976), Wilkinson and Malik (1987), Savas (1987) and, more recently, Schouveiler et al. (1999). Their wavelength, orientation angle and critical Reynolds number are given in Table 1. A review of Ekman boundary

Table 1
Experimental and theoretical data in source-sink rotating flows

Reference	Wave type	Ro	Re_c	λ/δ	ψ	v_ψ/v_g
Measurements						
Tatro and Mollö-Christensen (1967)[a]	I	–	$124.5 + 7.32Ro$	11.8	15°	0.034
Tatro and Mollö-Christensen (1967)	II	–	$56.3 + 116.8Ro$	27.8 ± 2	0° to −8°	0.16
Caldwell and Van Atta (1970)	II	–	56.7 ± 3	–	–	–
Weidman (1976)	II	–	60	20.4 ± 2.4	−1° to −7°	–
Theory						
Faller and Kaylor (1966)	I	0	118	11	10° to 12°	0.33
Faller and Kaylor (1966)	II	0	55	24	−15°	0.5
Lilly (1966)	I	0	110	11.9	8°	0.094
Lilly (1966)	II	0	55	21	−10°	0.57
Marlatt and Biringen (1995)	II	0	150	23	−10°	0.296
Two-dimensional numerical simulations						
Crespo del Arco et al. (1996)	II	$0.4 < Ro < 0.2$	74	29–26	0°	0.28

[a] These results have been criticized by Cesaroli (1975), who proved that these waves were induced by the measurement probe.

layer instabilities is available in the paper of Faller (1991) and a wide range of relevant nonlinear phenomena and instabilities within rotating flows are also reported by Hopfinger and Linden (1990).

In Crespo del Arco et al. (1996), we have confirmed and analyzed the axisymmetric instability that prevails at $R_m = 5$ (R_m is a characteristic curvature parameter, $R_m = (a+b)/\Delta R$) and the supercritical conditions as derived from Lilly's theoretical analysis valid in the limit of $Ro \to 0$. The purpose of the present study is to extend the analysis of the oscillatory transition to the regime of three-dimensional spiral patterns. The study uses a three-dimensional direct numerical simulation of the spatial and temporal modes that develop as a consequence of the boundary-layer instability in a rotating annular cavity. The configuration is subjected to a forced radial outflow originating at the inner cylindrical section. The flow is assumed to be isothermal and incompressible. High spatial resolution is a requisite to describe accurately the Ekman layers, especially for the numerical study of time-dependent motions. Spectral methods have been successfully applied to compute complex time-dependent flows (Canuto et al., 1988). We have used a spectral collocated Chebyshev method in the radial and axial directions and a Fourier–Galerkin azimuthally.

Our numerical simulations emphasize time-dependent patterns in a rotating frame of reference: axisymmetric and three-dimensional patterns, composed of circular rolls or spiral arms developing in the Ekman boundary layers. These structures are discussed and shown to be similar to the characteristic type II viscous instability. In the present configuration, multiple stable solutions can be obtained, all having similar wavelengths, revealing a problem of pattern selection. This corresponds to the intransitivity phenomenon observed during the study of baroclinic waves in differentially heated rotating annulii (Fowlis and Hide, 1965; Hignett et al., 1985). Circular waves are determined numerically but they are shown to be possibly very sensitive to the superposition of an azimuthal disturbance depending on the radius and on the modes of perturbation.

2. Formulation of the problem

The geometrical configuration is shown in Fig. 1. The radii of the annular cavity are a and b, with $a < b$, and the cavity height is $2h$. The geometrical parameters are the characteristic radius of curvature, defined as $R_m = (a+b)/\Delta R$, and the aspect ratio $L = \Delta R/(2h)$, where $\Delta R = b - a$.

The values of $R_m = 5$ and 10 are chosen in order to keep curvature effects reasonably low. Indeed, for more significant curvature effects ($R_m = 1.22$, $Ro = 0.36$), we have shown (Crespo del Arco et al., 1996) that the transition originates from an inertial instability in the entrance region that excited the Ekman layers. It was shown that this external perturbation

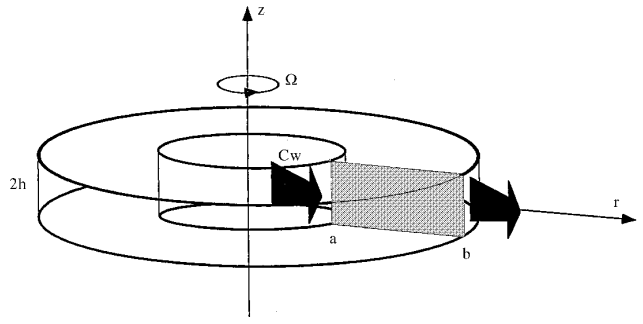

Fig. 1. Geometry and coordinate system.

provoked sub-critical modes of instability in the layers. These modes subsequently vanished over the characteristic spin-down time (Weidman, 1976) for C_w close to the critical value. For larger C_w, the combination of the two oscillatory behaviors was shown to be at the origin of a quasi-periodic behavior that precedes the transition to nonperiodic flow. In the present paper, the distance to the axis is increased and the relevance to the Ekman layer instability is studied, while considering directly an Ekman layer profile at the entrance and at the outlet of the rotating cavity. Thus, the curvature terms remain small and the Ekman profiles constitute a good estimate of the basic flow inside the cavity; this will be considered later in Section 5.

The aspect ratio of the cavity, $L = 3.37$, is taken so that the Ekman layer thickness is sufficiently small with respect to the height, yet allow for an extended geostrophic core. The length ΔR of the cavity is chosen so that a large number of instability wavelengths can form between the entrance and exit sections and also to constitute a good compromise with respect to the computational cost. Moreover, $L = 3.37$ is a relevant value for application to technological devices (Owen and Rogers, 1995) and for comparison with the fundamental laboratory experiments.

The cavity is rotating with uniform angular velocity $\Omega = \Omega \mathbf{e}_z$, $\mathbf{e}_z$ being the unit vector in the vertical direction. The scales for the dimensionless variables of space, time and velocity are $[h, \Omega^{-1}, \Omega b]$, respectively. The dimensionless spatial variables are denoted $(\bar{r}, \bar{z})$ and have been normalized to $[-1,1] \times [-1,1]$, a requirement for the use of Chebyshev polynomials. The normalized variables are denoted (r, z) with $r = \bar{r}/L - R_m$ and $z = \bar{z}$.

An important dimensionless parameter is the Ekman number. It is defined as $E = \nu/\Omega(2h)^2$ and characterizes the ratio δ/h, where $\delta = (\nu/\Omega)^{1/2}$ is the constant Ekman layer thickness and h is the half-height of the cavity. For sufficiently small values of E, the stability of both Ekman layers can be considered independently as in the flow over a single disk. As shown by fundamental analyses in the single infinite disk problem, the relevant parameter governing the onset of instability is the local Reynolds number, $Re = v_g^* \delta/\nu$, where v_g^* is the geostrophic velocity (see Section 5). Since the cavity begins at a finite distance a from the axis, we also have at our disposal a local Rossby number, defined by $Ro = v_g^*/\Omega r^*$, where r^* is the dimensional radial coordinate. The mass flow rate, Q, is made dimensionless according to $C_w = Q/\nu b$.

The flow is governed by the three-dimensional, incompressible Navier–Stokes equations, written in a rotating frame of reference, in the velocity $\mathbf{V} = (u, v, w)$ and pressure p formulation

$$\frac{1}{L}\frac{\partial u}{\partial r} + \frac{u}{L(r+R_m)} + \frac{1}{L(r+R_m)}\frac{\partial v}{\partial \theta} + \frac{\partial w}{\partial z} = 0,$$

$$\frac{1}{E}\frac{\partial u}{\partial t} + \frac{L(R_m+1)}{E}Au = -\frac{(R_m+1)}{E}\frac{\partial p}{\partial r} - \frac{8}{E}v + \left[\Delta u - \frac{u}{L^2(r+R_m)^2} - \frac{2}{L^2(r+R_m)^2}\frac{\partial v}{\partial \theta}\right],$$

$$\frac{1}{E}\frac{\partial v}{\partial t} + \frac{L(R_m+1)}{E}Av = -\frac{(R_m+1)}{E(R_m+r)}\frac{\partial p}{\partial \theta} - \frac{8}{E}u + \left[\Delta v - \frac{v}{L^2(r+R_m)^2} + \frac{2}{L^2(r+R_m)^2}\frac{\partial u}{\partial \theta}\right],$$

$$\frac{1}{E}\frac{\partial w}{\partial t}+\frac{L(R_{\mathrm{m}}+1)}{E}Aw=-\frac{L(R_{\mathrm{m}}+1)}{E}\frac{\partial p}{\partial z}+[\Delta w]$$

in which the advection terms are given by

$$Au=\frac{1}{L}u\frac{\partial u}{\partial r}+\frac{v}{L(R_{\mathrm{m}}+r)}\frac{\partial u}{\partial \theta}+w\frac{\partial u}{\partial z}-\frac{v^2}{L(r+R_{\mathrm{m}})},$$

$$Av=\frac{1}{L}v\frac{\partial v}{\partial r}+\frac{v}{L(R_{\mathrm{m}}+r)}\frac{\partial v}{\partial \theta}+w\frac{\partial v}{\partial z}+\frac{vu}{L(r+R_{\mathrm{m}})},$$

$$Aw=\frac{1}{L}u\frac{\partial w}{\partial r}+\frac{v}{L(R_{\mathrm{m}}+r)}\frac{\partial w}{\partial \theta}+w\frac{\partial w}{\partial z}$$

and the cylindrical Laplacian operator is

$$\Delta=\frac{1}{L^2}\frac{\partial^2}{\partial r^2}+\frac{1}{L^2(R_{\mathrm{m}}+r)}\frac{\partial}{\partial r}+\frac{1}{L^2(R_{\mathrm{m}}+r)^2}\frac{\partial^2}{\partial \theta^2}+\frac{\partial^2}{\partial z^2}.$$

The boundary conditions are rigid walls at $z=\pm 1$ and Ekman boundary layer profiles ((5.2) and (5.3)) are considered as inflow and outflow conditions at $\bar{r}=L(R_{\mathrm{m}}\pm 1)$, respectively (see Section 5).

3. Numerical method

The solution method is based on a pseudo-spectral Chebyshev–Fourier method (see Canuto et al., 1988). The choice takes into account the adequacy of the properties of Chebyshev orthogonal polynomial expansions and, in particular, of the exponential convergence, referred to as spectral accuracy (Gottlieb and Orszag, 1977). Moreover, the use of the Gauss–Lobatto collocation points, corresponding to the extrema of the Chebyshev polynomials of higher degree, N and M in the radial and axial directions, respectively, directly ensures high accuracy of the solution inside the very thin wall layers.

The differential equations are exactly satisfied at the Gauss–Lobatto collocation points, $(r_i,z_j)\in[-1,1]\times[-1,1]$

$$r_i=\cos\left(\frac{i\pi}{N}\right),\qquad z_j=\cos\left(\frac{j\pi}{M}\right),$$
$$(i=0,\ldots,N,\ j=0,\ldots,M).$$

The approximation of any flow variable $\Psi=(u,v,w,p)$ and its derivatives is derived from the truncated series representation

$$\Psi_{NMK}(r,z,\theta,t)=\sum_{p=K/2}^{K/2-1}\sum_{n=0}^{N}\sum_{m=0}^{M}\widehat{\Psi}_{nmp}(t)T_n(r)T_m(z)\mathrm{e}^{\mathrm{i}p\theta}$$
$$\text{for } -1\leqslant r,\ z\leqslant 1,\ 0\leqslant\theta\leqslant 2\pi$$

$$\frac{\partial^q\Psi_{NMK}}{\partial r^q}(r_i,z_j,\theta_k,t)=\sum_{\eta=0}^{N}\mathrm{d}r_{i\eta}^{(q)}\Psi_{NMK}(r_\eta,z_j,\theta_k,t),$$

$$\frac{\partial^q\Psi_{NMK}}{\partial z^q}(r_i,z_j,\theta_k,t)=\sum_{\xi=0}^{M}\mathrm{d}z_{j\xi}^{(q)}\Psi_{NMK}(r_i,z_\xi,\theta_k,t),$$

where $\mathrm{d}r_{ij}^{(q)}$ and $\mathrm{d}z_{ij}^{(q)}$ correspond to the coefficients of the matrix of first and second derivatives ($q=1,2$) and where $\theta_k=2\pi k/K$, $k=0\ldots,K-1$. An expansion of these coefficients based on sine functions (Rothman, 1991) is used to reduce the round-off error. T_n and T_m are the Chebyshev polynomials and $\widehat{\Psi}_{nmp}$ are the spectral coefficients defined by

$$\widehat{\Psi}_{nmp}(t)=\frac{1}{K}\frac{1}{c'_n}\frac{1}{c'_m}\sum_{k=0}^{K-1}\sum_{i=0}^{N}\sum_{j=0}^{M}\times\frac{1}{c_ic'_j}\Psi(r_i,z_j,\theta_k,t)T_n(r_i)T_m(z_j)\mathrm{e}^{-\mathrm{i}p\theta_k}$$

with $c_0=c_N=c'_0=c'_M=2$ and $c_n=c'_m=1$ for $n=1,\ N-1$ and $m=1,\ M-1$. The unknowns $\Psi(r_n,z_m,\theta_k)$ are required to be real in physical space. The physical conditions are explicitly taken into account at the boundaries.

The time scheme is semi-implicit and second-order accurate. It corresponds to a combination of a second-order backward differentiation formula for the diffusive term and the Adams–Bashforth scheme for the nonlinear terms (see Vanel et al., 1986). The velocity–pressure coupling is performed with an efficient projection algorithm developed in Hugues and Randriamampianina (1998) (see Hugues, 1998). It corresponds to an improved version of the approach proposed by Goda (1979) and implemented by Gresho and Sani (1987) to finite elements and by Raspo (1996) to three-dimensional spectral approximation. It consists of introducing a correct predictor for the pressure, directly derived from the Navier–Stokes equations, which provides an appropriate consistent pressure field with a divergence-free velocity. This procedure allows a possible temporal evolution of the normal gradient of pressure at the boundaries, known to be the main drawbacks of the initial projection scheme. Moreover, this modified algorithm is shown to reduce the slip-velocity on the boundaries by one order of magnitude (compared to that of the temporal scheme) and it improves the incompressibility condition without the need of a staggered grids for the velocity and the pressure. At each time step, the solution of the Navier–Stokes equations reduces to a solution of Helmholtz and Poisson type equations in the Fourier space. A direct solver for these equations is used, based on a complete matrix diagonalization technique proposed by Haldenwang et al. (1984); for this configuration the matrices of radial and axial operators are diagonalizable with real eigenvalues.

Note that an extension of this numerical method in the case involving the axis ($\bar{r}=0$) is proposed elsewhere in Serre and Pulicani (2000).

4. Numerical details

Computations were performed with spatial resolutions of $N\times M\times K=48\times 48\times 48$ to $48\times 48\times 128$, where N and M are the number of Chebyshev polynomials in the axial and radial directions and K the number of the Fourier modes used in the azimuthal expansion. The former axisymmetric study in a rotating annular cavity of Crespo del Arco et al. (1996) indicates that a spatial resolution of 48×48 in (r,z) for the considered geometrical (R_{m},L) and physical (E,C_{w}) parameters, constitutes a good compromise between accuracy and computational cost. The time step used in the computations is governed by the spatial resolution in (r,z), $\Delta t=4.0\times 10^{-3}$. The time considered for each solution was sized on the largest characteristic time in rotating flows (Greenspan, 1969), the viscous time $t_{\mathrm{v}}=E^{-1}$ ($\cong$450 in present cases); over this very large time scale, the viscous diffusion has already affected the entire core of the cavity and the small residual inertial oscillations are strongly damped.

Convergence to steady state is assumed to be achieved when the convergence rate becomes smaller than a relevant value that is taken in our study as $|\mathbf{V}^{n+1}-\mathbf{V}^n|/\delta t\leqslant 10^{-5}$, where $\mathbf{V}$ is the velocity vector, and the superscripts $n+1$ and n correspond to the time stages $(n+1)\delta t$ and $n\delta t$. The solution strategy then consists of initializing the computation at larger

C_w with the solution formerly obtained at a lower value of C_w, the rotation rate being constant ($E = 2.24 \times 10^{-3}$).

5. Basic flow

The basic flow solution is stationary and axisymmetric and corresponds to the Ekman layer flow. The meridianal velocity field of the basic solution is displayed in Fig. 2(a) for $0 < z \leqslant 1$ and for $C_w = 200$. The radially outward flows that develop parallel to the walls dominate the weak reverse flows observed at the edge of the boundary layers bordering the geostrophic core; details of the structure of the radial velocity profile at mid-section are given displayed in Fig. 3(a). For large values of the mass flow rate C_w, vortex structures are superimposed on each layer close to the disks; see Fig. 2(b) computed for $C_w = 530$ and plotted for $-1 \leqslant z \leqslant 0$. At $R_m = 5$, the solution remains steady and axisymmetric below $C_w \cong 460$ at $E = 2.24 \times 10^{-3}$ and the Ekman boundary layer flow is stable. For this type of flow, the Coriolis force dominates with respect to inertial and centrifugal forces near the walls ($E \ll 1$ and $Ro \ll 1$). Then, in a frame of reference rotating with the walls at angular velocity Ω, the Navier–Stokes equations can be approximated by (Greenspan, 1969)

$$-(v - v_g) = 4E\frac{\partial^2 u}{\partial z^2}, \tag{5.1}$$

$$u = 4E\frac{\partial^2 v}{\partial z^2}$$

with the boundary conditions $u = v = 0$ at $z = \pm 1$ and $u \to 0$, $v \to v_g$ when $z \to 0$. The isothermal flow organizes itself symmetrically and parallel Ekman layer flows form on the two disks with the same mass flow rate. Solutions across the height of the cavity can be derived from Eq. (5.1) with the above boundary conditions. The axial velocity is $w = 0$ (parallel flow assumption) and the radial and azimuthal components are, respectively,

$$u = v_g\{\exp[-E^{-1/2}(z+1)]\sin[-E^{-1/2}(z+1)] - \exp[E^{-1/2}(z-1)]\sin[E^{-1/2}(z-1)]\}, \tag{5.2}$$

$$v = -v_g\{1 - \exp[-E^{-1/2}(z+1)]\cos[-E^{-1/2}(z+1)] - \exp[E^{-1/2}(z-1)]\cos[E^{-1/2}(z-1)]\}, \tag{5.3}$$

where v_g is a function of the radius and corresponds to the dimensionless azimuthal velocity of the inviscid geostrophic flow between the two viscous Ekman layers (Hide, 1968)

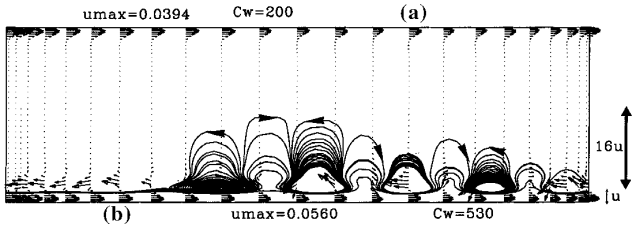

Fig. 2. Display of the velocity field (u, w) in the meridianal plane (r, z) in the cavity $L = 3.37$, $R_m = 5$, and at $E = 2.24 \times 10^{-3}$. Two zones are emphasized: one below near the wall and the second in the core, where the velocity is displayed with a factor 16. The vortices are emphasized by paths of markers introduced in the near entry region at left. (a) In the upper half part, $0 < z \leqslant 1$, steady basic flow solution for $C_w = 200$; reference scale is $u_{max} = 0.0394$. (b) In the lower part, $-1 \leqslant z \leqslant 0$, unstable flow solution for $C_w = 530$; reference scale is $u_{max} = 0.0560$.

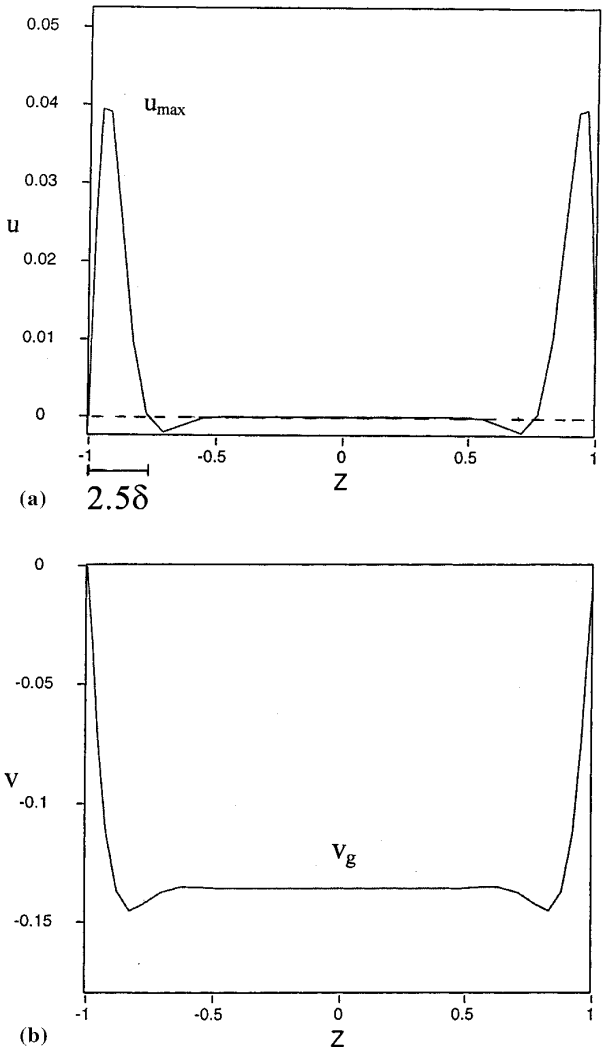

Fig. 3. Basic flow solution at $C_w = 200$, $E = 2.24 \times 10^{-3}$; z-profiles of the velocity at the middle section of the cavity $\bar{r} = LR_m$ $(r = 0)$, $L = 3.37$, $R_m = 5$. Characteristic length and velocity scales (refer to Hide, 1968). (a) Radial component of the velocity, u; (b) azimuthal component of the velocity, v.

$$v_g = \frac{C_w E^{1/2}}{2\pi L(R_m + r)}. \tag{5.4}$$

In the numerical solution at $C_w = 200$, the predominant meridianal flow appears in these two Ekman layers (see the radial velocity profile in Fig. 3(a)); outside these Ekman layers, in the geostrophic core, the Coriolis force balances the pressure gradient and the flow is predominantly azimuthal. In this geostrophic region, both the radial and the axial velocities are small and the flow rotates inside the cavity at a slower rate than the walls (see the azimuthal velocity profile in the rotating frame of reference, Fig. 3(b)). The thicknesses of the Ekman layers are referred to as δ and the azimuthal core velocity is denoted the geostrophic velocity v_g (see Hide, 1968, for theoretical results).

The solutions (5.2) and (5.3) used as inflow (at $\bar{r} = L(R_m - 1)$) and outflow (at $\bar{r} = L(R_m + 1)$) boundary conditions appear as natural boundary conditions at this distance from the axis ($R_m \geqslant 5$) for the considered rotation rate ($E = 2.24 \times 10^{-3}$). For larger values of the mass flow rate C_w, this solution also represents a good average approximation of

the velocity field in the whole cavity. For example, the geostrophic velocity varies similarly to Eq. (5.4) and this expression underestimates by less than only 5% the actual geostrophic velocity numerically obtained inside the cavity, $L(R_m - 1) < \bar{r} < L(R_m + 1)$, at $C_w = 530$; the time-averaged geostrophic velocity is about $v_g = 0.243$, while the value from the analytical solution (5.4) is $v_g = 0.238$. Moreover, we note that there is no evidence of inertial effects at the entrance and exit regions, as was analytically determined elsewhere by Hide (1968) and simulated by Crespo del Arco et al. (1996).

6. Results and analysis

The results presented in this section were obtained for an aspect ratio $L = 3.37$, a constant rotation rate, $E = 2.24 \times 10^{-3}$, and a mass flow rate C_w between 460 and 600 in order to be in a range of local parameter values, (Re, Ro), characteristic of the type II instability. Using the zero-order solution for the azimuthal velocity (5.4), the Reynolds and Rossby numbers at a given position $r \in [-1; 1]$, are $Re = C_w(R_m + 1)/[2\pi(R_m + r)]$ and $Ro = C_w E^{1/2}(R_m + 1)/2\pi L(R_m + r)^2$.

In order to identify and study the spatial structure of the instabilities, which develop in each of the two boundary layers, one uses the axial velocity component, which is nearly zero in the Ekman layer flow and constitutes a very sensitive marker to local disturbances. The dynamical behavior was investigated by noting the time history of the variables (u, v, w, p) in the Ekman layers and in the geostrophic region at two principal locations: $(r_1, z_1, \theta_1) = (0, 0.98, \pi/4)$ and $(r_2, z_2, \theta_2) = (0, 0, \pi/4)$ for $(r, z, \theta) \in [-1; 1] \times [-1; 1] \times [0; 2\pi]$. Some relevant experimental and numerical results together with results of a stability analysis are listed in Table 1.

6.1. Axisymmetric patterns

The initial condition is the computed solution of the time-dependent Navier–Stokes equations at $C_w = 460$ and $E = 2.24 \times 10^{-3}$. This stable solution is axisymmetric and similar to the solution displayed in Fig. 2(a) (above, $0 < z \leqslant 1$ for $C_w = 200$). When increasing the mass flow rate, $C_w = 530$, a Hopf bifurcation is exhibited to a periodic oscillatory solution and the flow is still axisymmetric (Fig. 4). After a transient time $t = 4$ (which is about $t_E/3$, where t_E is the characteristic Ekman time, $t_E = h/(v\Omega)^{1/2}$ (Greenspan, 1969), the frequency of the oscillation plotted in Fig. 4(b) is $\sigma = 7.4$, where σ is scaled with the rotation rate Ω). We obtain good agreement between the computed value of σ and the frequency reported from experiments by Caldwell and Van Atta (1970), far from the critical Reynolds number and for $Ro \neq 0$. For Re in the range of $110 \leqslant Re \leqslant 250$, these authors notice a linear dependence of the frequency, $7 \leqslant \sigma \leqslant 12$. Herein, the values of the Reynolds and Rossby numbers are given using the computed velocity at the center of the cavity, in this case, $Re = 102$ and $Ro = 0.29$.

Results of the numerical solution displayed in Fig. 4(a) exhibit six pairs of counter-rotating axisymmetric rolls in the Ekman layer traveling radially outward with phase velocity v_ψ of about $v_\psi/v_g = 0.28$. The contour-lines of the axial velocity in Fig. 4(a) emphasize the deflection to the parallel flow in the Ekman layers. The structures of limited magnitude superimpose to both the Ekman layers (where the parallel flow is radial) and the geostrophic core (corresponding to solid body rotation) extending to the center of the cavity. However, the pattern only displays the flow disturbance and the flow zones remain the same than in the steady flow.

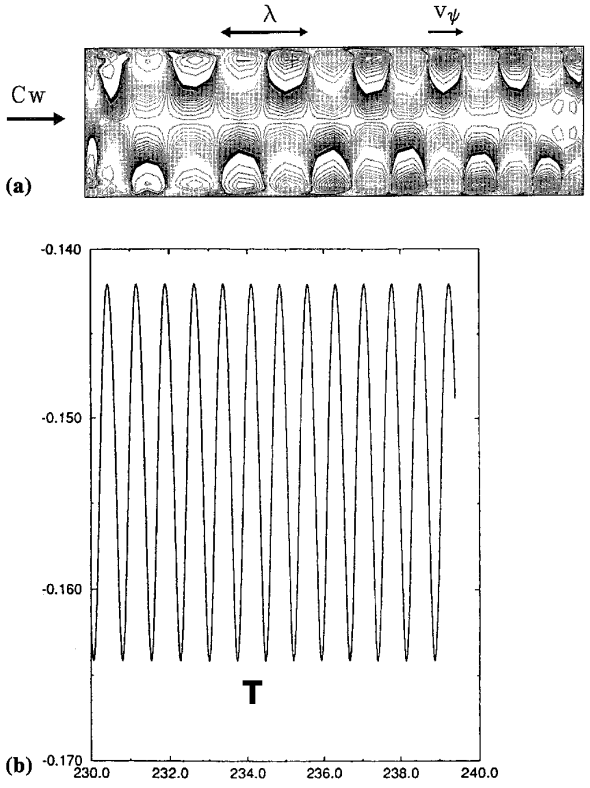

Fig. 4. Axisymmetric instability at $C_w = 530$, $E = 2.24 \times 10^{-3}$ and at $R_m = 5$. Characteristic wavelength λ, phase velocity v_ψ, and frequency $\sigma = 2\pi/T$. (a) Instantaneous iso-lines of the axial velocity component in the meridianal flow $(r, z, \pi/4)$. Visualisation of six pairs of counter-rotating vortices, at $t = 250$, $N \times M \times K = 48 \times 48 \times 48$. (b) Time history of the azimuthal component of the velocity v in $(r, z, \theta) = (0, 0.95, \pi/4)$. Periodic behavior with $\sigma = 7.4$. The major disturbances (inner circles) are separated from the weaker disturbances (outer circles) extending in the core, by a blank zone.

In Fig. 2(a), the velocity vector field is divided into two zones: the near wall, where the main flow is concentrated under the form of the Ekman layers and where the maximum velocities are located; the rest of the cavity, where the flow is very weak in the meridian plane. The length scale for the velocity vector refers to the maximum in the Ekman parallel flow profile. The velocity vectors in the geostrophic region are magnified by a factor of 16. Then, these velocity vectors displayed in the core with a same magnitude, indeed correspond to a velocity smaller by a factor of 16 with respect to the ones in the Ekman layer. We note that the instability mainly locates at the border between the Ekman layer and the geostrophic core: the disturbances are of small amplitude but we can isolate their expansion by injecting adequately the particles in the interesting zone before tracking them as markers of the instability structures. The vortices localization is emphasized by using particle paths originating from the entrance region bordering the wall region and the core.

The wavelength in the radial direction is defined as $\lambda_r = \Delta R/n_r$, n_r being the number of pairs of vortices along the radius ($n_r = 6$); the wavelength is sized in terms of the scale length of the Ekman layer, δ, as is usual in the literature. The wavelength is roughly constant at about $\lambda_r = 24\delta$, slightly decreasing from 26δ to 23δ between the entrance and the exit sections.

These results are similar to the axisymmetric solution obtained in two dimensions in an earlier paper by Crespo del

Arco et al., 1996 (see Table 1) with a different numerical method (streamline-vorticity formulation) at $C_w = 467$ and $E = 2.24 \times 10^{-3}$. Moreover, good agreement with the theoretical results at $Ro = 0$ is obtained (see Table 1). To our knowledge, this axisymmetric mode of instability has never been noticed in experimental studies of the Ekman layer in which mainly spiral structures are obtained. Nevertheless, our solution is quite similar to the experimental results in the Bödewadt layer on a stationary disk. Savas (1987) was the first to observe, in an enclosed rotor–stator cavity, traveling circular waves during impulsive spin-down to rest, $25 \leqslant Re \leqslant 125$, with a frequency of $\sigma = 5$. He observed nine pairs of rolls with an average radial wavelength of $\lambda_r = 20\delta$.

The range of the parameters $(\lambda_r, \sigma, v_\psi)$ is characteristic of the axisymmetric mode of the type II Ekman boundary-layer instability.

6.2. Three-dimensional spiral patterns

The rolls that progress in the form of rings in the axisymmetric solution, now constitute spiral expanding outwards inside the cavity. The orientation of the wave front is measured by the angle ε with respect to the azimuthal direction. It is defined positive when it is rolled up towards the axis of the disk in the rotation direction.

Due to the high level of accuracy of the spectral solution (the round-off errors and hence the numerical noise are very small) and due to the cost of CPU time, the transition to three-dimensional patterns was not actually carried out over very large time intervals, but the process was accelerated by considering "artificial" initial disturbances. This axisymmetric flow was perturbed by superimposing a disturbance at a given instant to the azimuthal velocity of general form $\alpha v \sin(p\theta)$ where p is an arbitrary number corresponding to an azimuthal wavelength and α the amplitude growth rate. The disturbance is introduced near the entrance section. The divergence free constraint is satisfied after a few preliminary iterations. In addition, the same results have been obtained after perturbing similarly the two other velocity components. Disturbances of different amplitude rates are shown to give exactly the same spiral flows but the transient time to reach the stable state noticeably depends on α. We have estimated the transitory time by perturbing the same axisymmetric nonlinear Ekman solution with various amplitude rates $\alpha = 0.008$, 0.02 and 0.05. The results give a dependency of this transitory time with a growth rate which behaves roughly as $\alpha^{-1/3}$. The significant time histories of the axial velocity component inside the Ekman layer are shown in Figs. 5(a)–(c) for $C_w = 530$, $E = 2.24 \times 10^{-3}$ for the three values of the amplitude rate α.

In previous work, Hugues et al. (1998), we already observed that the radial component of the wave number in spiral patterns remains exactly the same as in the circular patterns; six pairs of rolls travel outwards, near both disks. However, in these structures an azimuthal component also arises. The azimuthal wavelength is defined as $\lambda_\theta = 2\pi\bar{r}/n$, n being the number of spiral arms over 2π. The general wavelength of the spiral patterns can be defined by λ, as $\lambda = (2\pi\bar{r}/n)|\sin\varepsilon|$.

Fig. 6 shows multiple solutions of spiral instability patterns at the fixed parameter values $C_w = 530$, $E = 2.24 \times 10^{-3}$ and $R_m = 5$. The multiplicity appears in the different numbers of spiral arms following the periodicity of the disturbances, $n \geqslant p, p \geqslant \Delta R/\lambda_r (\approx 6)$ as shown in Fig. 6(d). These solutions, for example the ones displayed in Figs. 6(a)–(c), are stable to further disturbances with $p \neq n$. The characteristics of the stable solutions are given at the center of the cavity in Table 2. The angle ε between the geostrophic and the phase velocity, is taken at the center of the cavity, $\bar{r} = LR_m$, and is negative in each case. The wavelength of the spiral waves varies slightly with the number of spiral arms and is about 25δ at $\bar{r} = LR_m$, diminishing with the radial location; for $n = 6$, λ decreases in the range of $19.7 \leqslant \lambda/\delta \leqslant 29.5$. All the solutions are periodic with a frequency slightly larger than for the axisymmetric solution. A second transient frequency modulates the time signal and its value is estimated between $\sigma \simeq 0.4$ and 1.7, depending on the periodicity of the initial disturbance, p. During the integration time (over about one viscous time), the modulation significantly damps and has almost disappeared at the end of the simulation. The modulation is interpreted to be a result of the inertial waves excited by the disturbances at the initial time. We display the dispersion relation $\sigma = \sigma(n)$ in Fig. 7; the angular frequency is shown to increase with the number of arms, i.e., $\sigma \propto n$.

In Figs. 8(a)–(c), we present a three-dimensional display of the w iso-surfaces after projection on a rectangular reference frame, which exhibits the expansion of 6–12 spiral arms, $n = 6, 8, 12$, over π radians in the azimuthal direction, that is over half of the domain. In order to emphasize the vortex structures, we have graphically displayed various points of view that illustrate the inclination with respect to the azimuthal direction.

The phase velocity of circular waves behaves as $1/\bar{r}$ (Crespo del Arco et al., 1996). The spiral wave fronts propagate in the azimuthal direction with a dimensionless angular velocity $\omega = \sigma\ n^{-1}$. As the radial component of the phase velocity varies as $A/\bar{r}$ (A is a constant), the velocity of the wave front is $(v_{\psi_r}, v_{\psi_\theta}) = (A/\bar{r}, \omega\bar{r})$. A generic equation of the wave front can easily be derived from the condition of colinearity between the displacement of the instability and the phase velocity. The polar equation is derived as $\bar{r}^2 = 2A\omega^{-1}(\theta + \beta_i)$ where β_i is a constant which depends on the number of spiral arms. In the numerical solutions, we obtained six pairs of vortices that expand radially following a number of spiral arms which is greater or equal to six (refer to Fig. 6(d)). Each spiral arm originates at the inner radius, $\bar{r} = L(R_m - 1)$, and terminates at $\bar{r} = L(R_m + 1)$ through an angle of 2π for six arms, of $3\pi/4$ for eight arms (see Figs. 6(a) and (b)) and more generally, of $12\pi/n$ with n arms, $n \geqslant 6$. Using these results we determine the constant A and the wave front can then be expressed as

$$\bar{r}^2 = \frac{nLR_m}{3\pi}\left(\theta + \frac{2\pi i}{n}\right). \tag{6.1}$$

The angle of the wave front with the geostrophic velocity thus varies as r^{-2} following:

$$\tan\varepsilon = -\frac{v_r}{v_\theta} = -\frac{nR_m}{6\pi(R_m + r)^2}$$

and is given in Table 2 at the center of the cavity, $\bar{r} = LR_m$. The dimensionless phase velocity v_ψ/v_g is nearly independent of the radial coordinate for the range of r-values considered.

These three-dimensional spiral patterns have been observed in the experiments of the Ekman layer (see the review in Faller, 1991; Crespo del Arco et al., 1996). The characteristic parameters are in good agreement with those obtained in the relevant experiments (see Table 1). Caldwell and Van Atta (1970) and Faller and Kaylor (1966) found in experiments similar structures that they referred to as type II instabilities of the Ekman layer. Faller and Kaylor (1966) observed spiral arms for a critical Reynolds number $Re \approx 70$ (while our value is $Re = 85$) with a wavelength close to those obtained in the present computations, in the range of $22 \leqslant \lambda/\delta \leqslant 33$, decreasing with radial location and with spiral angles in the range $-20° \leqslant \varepsilon \leqslant 5°$. Moreover, the present results are quite similar to those given by the stability analyses for $Ro = 0$ in the case of

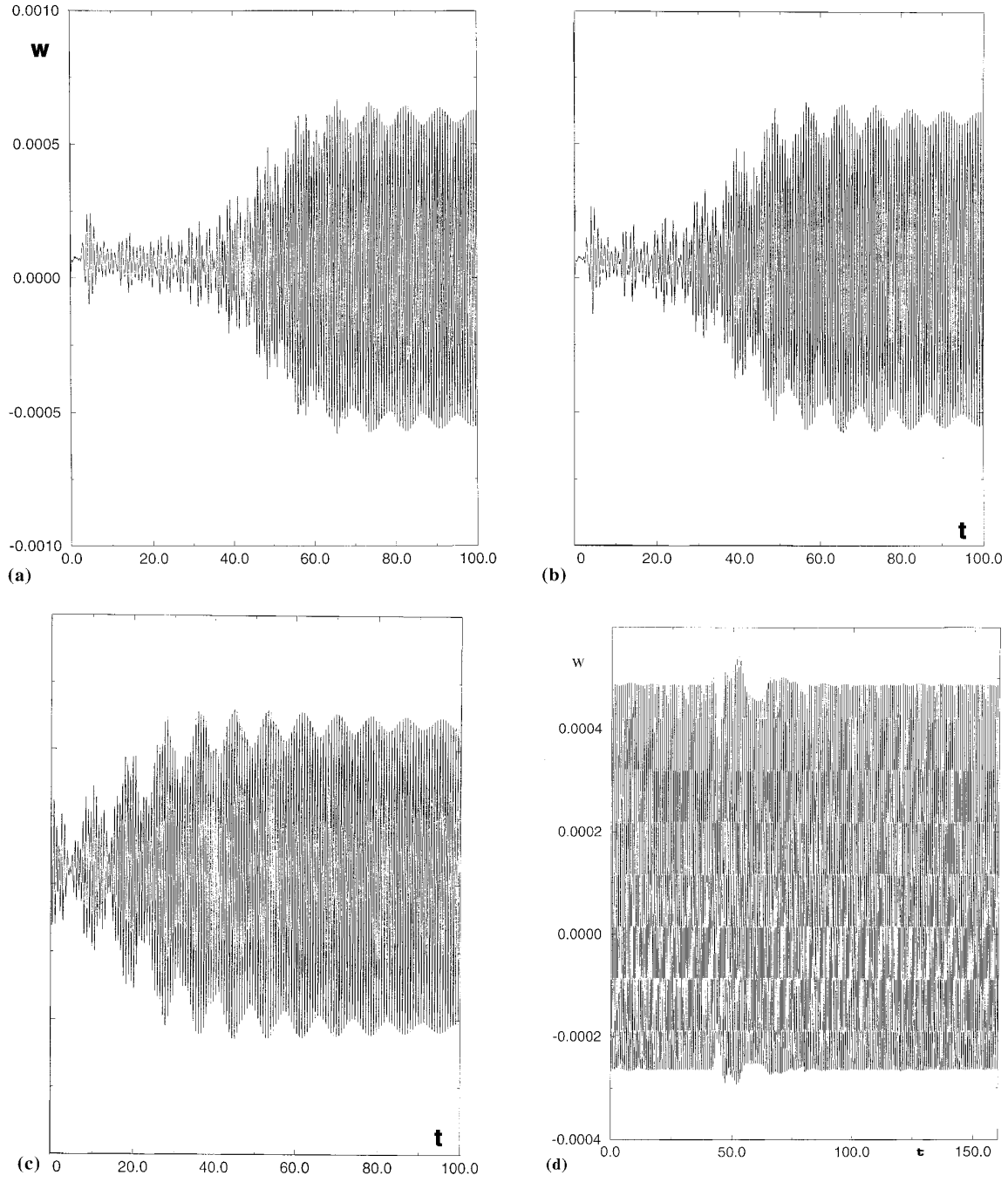

Fig. 5. Time history of the axial velocity component in $(r, z, \theta) = (0, 0.95, \pi/4)$ at $E = 2.24 \times 10^{-3}$. Amplification of azimuthal disturbance ($p = 12$) on the nonlinear Ekman solution at $C_w = 530$ and at small radius $R_m = 5$: (a) $\alpha = 0.002$, (b) $\alpha = 0.02$, (c) $\varepsilon = 0.05$. (d) Damping of the disturbance ($p = 3$) on the oscillatory axisymmetric solution at $C_w = 600$ and at large radius $R_m = 10$, for a larger magnitude rate $\alpha = 0.1$.

an infinite disk. Faller (1991) obtained an instability characterized by spiral arms of wavelength $\lambda = 20.1$ and forming an angle $\varepsilon = -23.1°$. We conclude, therefore, that the spiral structure of the computed rotor layer shows the same characteristics as the type II viscous instability of the Ekman layer.

6.3. Curvature effects

Spiral waves have been found in spin-down experiments at intermediate radii of curvature. At large radii, the wave front is nearly flat and travels following a direction which makes a constant angle with the geostrophic velocity. In order to provide a perspective on the fact that spiral waves are a result of the radius of curvature (smaller values of the radius correspond to large values of the Rossby number), we have computed the solution for lower curvature effects considering a curvature parameter $R_m = 10$. The dimensionless mass flow rate is $C_w = 600$ that corresponds to local values of Re in the range $95.5 \leqslant Re \leqslant 105$ for $R_m = 10$, which are very close to the case $R_m = 5$ ($84.4 \leqslant Re \leqslant 126.5$). At the center of the cavity the Rossby number is equal to $Ro = 0.15$, that is twice smaller

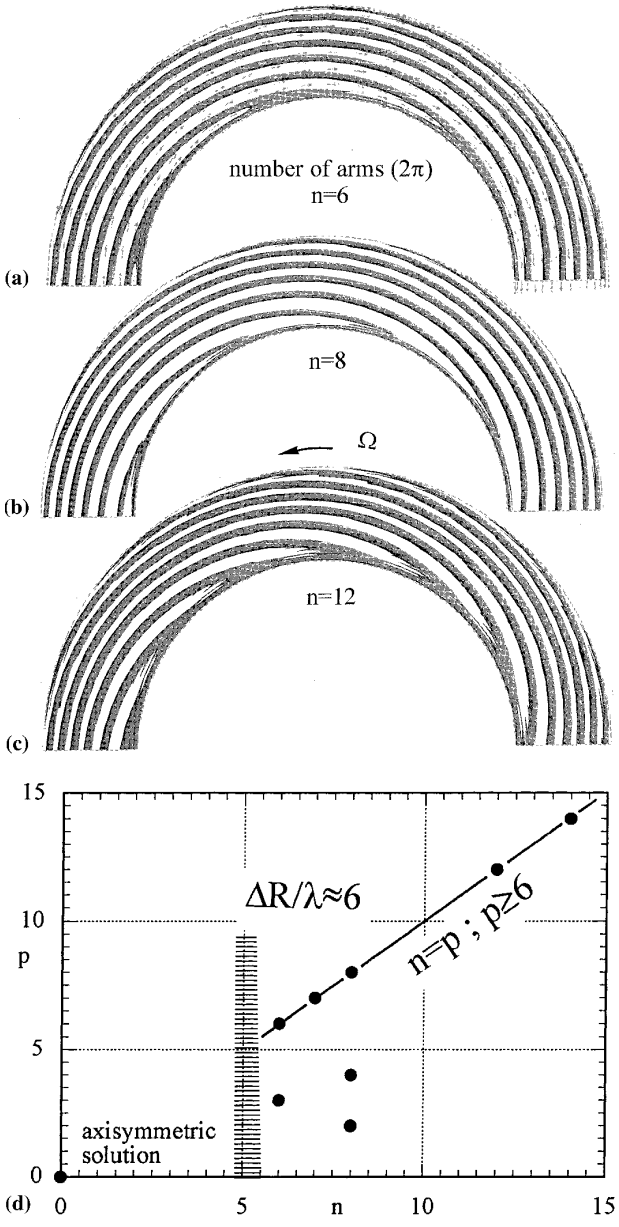

Fig. 6. Three-dimensional displays of instantaneous iso-surface of the axial velocity component, for $0 < z \leqslant 1$, projected in a plane (r, θ), $0 \leqslant \theta \leqslant \pi$; at $t = 250$, $N \times M \times K = 48 \times 48 \times 64$, for $C_w = 530$, $E = 2.24 \times 10^{-3}$ and at $R_m = 5$. The cavity rotates in the anti-clockwise direction. (a) Spiral patterns of the instability with six arms, and velocity field in the geostrophic region $(r, z = 0, \theta)$. (b) Spiral patterns with eight arms. (c) Spiral patterns with 12 arms. (d) Response of the system to disturbance. Minimal number of pairs of arms, $n \geqslant \Delta R/\lambda_r$ (≈ 6); multiple solutions from various disturbances of periodicity varying from 2 to 14.

than $Ro = 0.29$ at $R_m = 5$ (the linear solution corresponds to $Ro = 0$).

The numerical solution is still axisymmetric, with six pairs of counter-rotating rolls, similar to the axisymmetric solutions obtained using $R_m = 5$. The solution is oscillatory in time with frequency $\sigma = 7.6$, with wavelength $\lambda = 24\delta$. We have disturbed this axisymmetric solution with periodic disturbances of $p = 3, 6, 14$ and with magnitudes α up to 0.1. For both $p = 3$ and $p = 6$, the amplitude decays (see Fig. 5(d)) and the final stable solution are the same axisymmetric oscillatory solution.

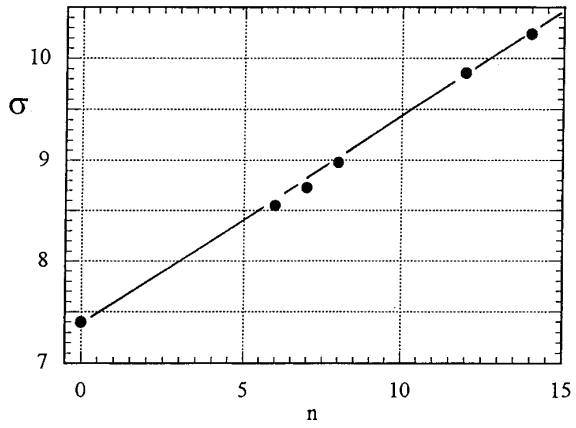

Fig. 7. Dispersion relation $\sigma = \sigma(n)$ for $C_w = 530$, $E = 2.24 \times 10^{-3}$ and at $R_m = 5$.

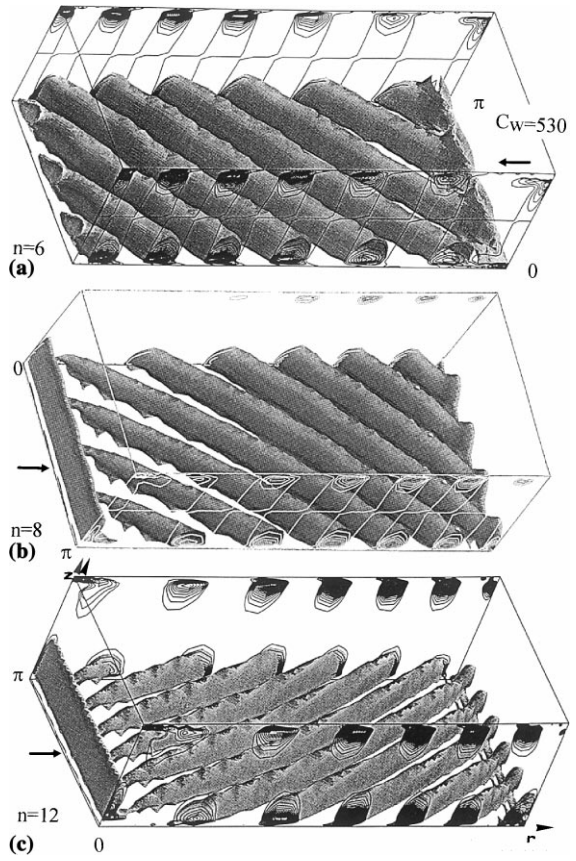

Fig. 8. Three-dimensional displays of instantaneous iso-surface of the axial velocity component in a cartesian reference frame, $0 \leqslant \theta \leqslant \pi$. Visualization of the six pairs of counter-rotating vortices in the meridianal plane (r, z); at $t = 250$, $N \times M \times K = 48 \times 48 \times 64$, for $C_w = 530$, $E = 2.24 \times 10^{-3}$ and at $R_m = 5$. (a) Spiral patterns with six arms. (b) Spiral patterns with eight arms. (c) Spiral patterns with 12 arms.

Unlike the original results for $R_m = 5$, the same perturbations, $p = 3$ and 6, provoked the rise of spiral patterns with 12 and 6 arms, respectively. However, the spiral wave solution with 14 arms remains a stable solution at both $R_m = 5$ and 10, both obtained from a $p = 14$ disturbance after simulation times of 250 and 150, respectively.

Table 2
Parameters of the three-dimensional solutions obtained with different disturbances ($\sin p\theta$) from the axisymmetric solution for $C_w = 533$ and $E = 2.24 \times 10^{-3}$. All the instability structures have the same radial wavelength (six vortices in the radial direction).

Number of arms, n	p	σ	ψ	v_ψ/v_g
Axisymmetric	–	7.4	0°	0.28
6	3,6	8.55	−3.64°	0.32
7	7	8.73	−4.25°	0.32
8	2,4,8	8.98	−4.85°	0.33
12	4,12	9.86	−7.26°	0.36
14	14	10.24	−8.45°	0.38

The spiral (and also the axisymmetric) waves can be characterized by the azimuthal component of the wavelength λ_θ. From the $R_m = 5$ ($p = 6$) and the $R_m = 10$ ($p = 14$) results, there exists an upper bound on the wavelength as the minimal number of arms increases roughly linearly with $\bar{r}$. This maximum wavelength does not change greatly in the range of the curvature parameter R_m. The axisymmetric solution is stable with respect to disturbances of azimuthal wavelengths, λ_θ, larger than roughly 5.3π, but it is unstable to azimuthal wavelengths smaller than 5.3π.

7. Discussion

Using Ekman layer profiles as boundary conditions at the source and at the sink in a rotating cavity at high rotation rate ($E = 2.24 \times 10^{-3}$) and with two moderate curvature parameters, $R_m = 5$ and 10, we have numerically investigated the type II Ekman layer instability using a three-dimensional Chebyshev–Fourier pseudo-spectral method. Below $C_w = 460$, $R_m = 5$, corresponding to $73.2 \leqslant Re \leqslant 110$, the solution remains steady and axisymmetric, composed of two Ekman layers close to the rotating walls separated by a geostrophic region with solid body rotation. When the mass flow rate is increased to $C_w = 530$ at $R_m = 5$ for which $84.4 \leqslant Re \leqslant 126.5$ and to $C_w = 600$ at $R_m = 10$ for which $95.5 \leqslant Re \leqslant 105$, the results of the numerical simulations reveal an oscillatory motion with frequencies in the range $7.4 \leqslant \sigma \leqslant 10.24$ associated with an axisymmetric mode of instability in the Ekman boundary layer. The circular patterns exhibited in Fig. 9(a) are similar to those obtained in experiments by Wilkinson and Malik (1987), Savas (1987), Schouveiler et al. (1999) and Weidman (1976) in the case of a Bödewadt boundary layer, and are shown to be sensitive to the superposition of disturbances. We notice that this axisymmetric mode of instability has never been observed in experimental studies of the Ekman layer formed in an annular geometry with radial throughflow.

Three-dimensional spiral structures also appear in the annular domain close to the rotating disks (Fig. 9(b)). From an analysis of our numerical results, we propose a generic equation (6.1) for the position of the wave front, depending on the curvature parameter R_m.

Moreover, we demonstrate that the circular wave instability develops at different radii of curvature and can remain stable with respect to the large wavelength of the azimuthal disturbances. In this study, the transition from axisymmetric to spiral rolls has not been observed without any initial disturbance, at least in the time of computation (about t_v) employed which we assume is sufficiently large. This means that for the same parameters, (R_m, Re, Ro), there are multiple nonlinear stable solutions, all stable to infinitesimal disturbances and

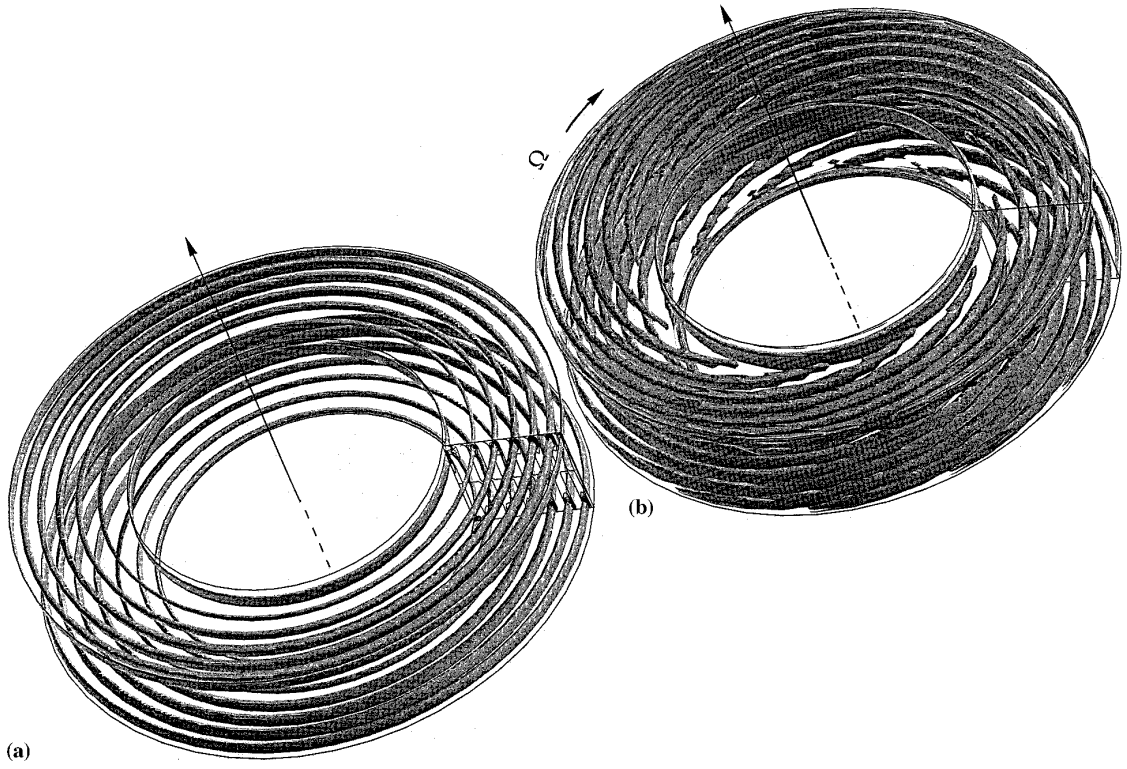

Fig. 9. Three-dimensional displays of instantaneous iso-surface of the axial velocity component in the annular domain. At $t = 250$, $N \times M \times K = 48 \times 48 \times 64$, for $C_w = 530$, $E = 2.24 \times 10^{-3}$ and at $R_m = 5$. (a) Circular patterns of the axisymmetric instability. (b) Spiral arms ($n = 12$) of the three-dimensional instability. The cavity rotates in the anti-clockwise direction.

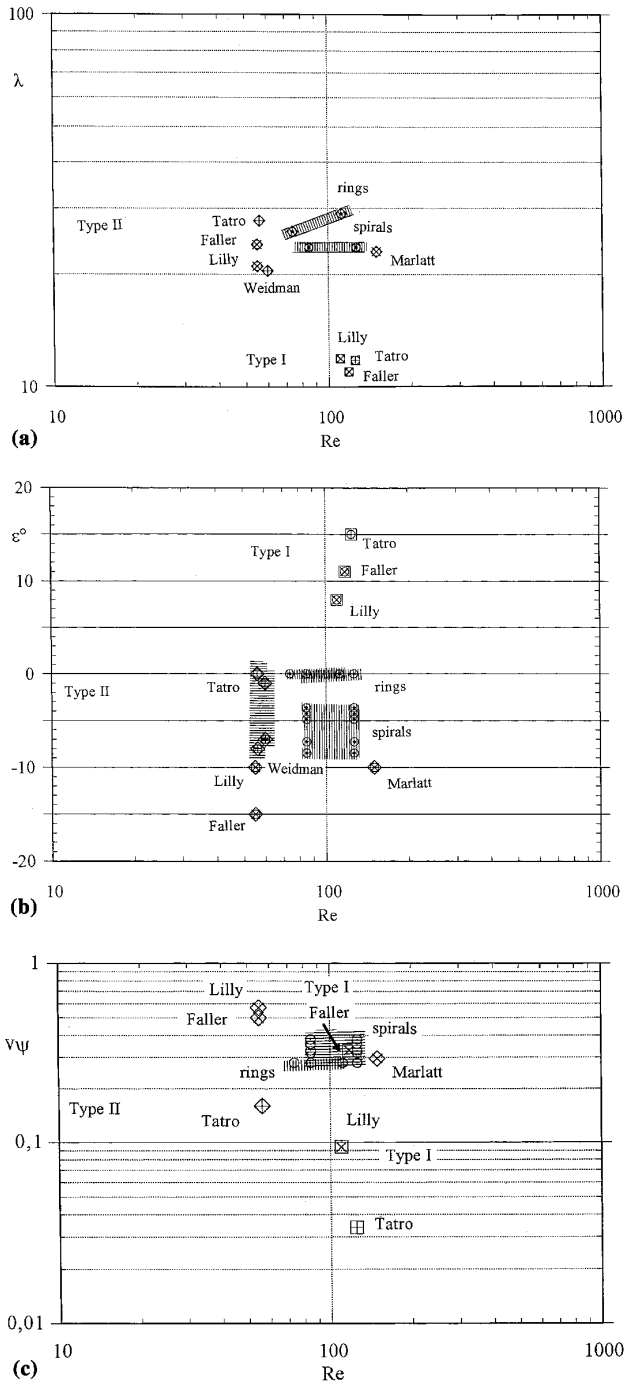

Fig. 10. Characteristic parameters of type I and type II instabilities from Tables 1 and 2 vs local Reynolds number, *Re*; experimental, theoretical and numerical values of: (a) the wavelength, λ, (b) the inclination angle, ε, (c) the phase velocity, v_ψ. Dashed zones represent the variation of the parameters with *Re* and the multiple spiral patterns.

appearing with different initial conditions. However, we have observed that the spiral patterns, once formed, do remain stable to further disturbances.

Different experimental observations have mentioned the existence of multiple stable solutions in rotating confined flows, known as the intransitivity phenomenon (Fowlis and Hide, 1965; Hignett et al., 1985). These studies were devoted to baroclinic waves in differentially heated rotating annulii. Both authors mentioned that such a behavior occurs during the transition from axisymmetric to three-dimensional flows before unique wave flow solution establishes. Hignett et al. (1985) have also carried out numerical investigations of these flows and obtained multiple three-dimensional solutions by introducing perturbations on the temperature field in axisymmetric solutions, similarly to the present process. The phenomenology of the situation with multiple solutions presents also some similarities with the stability (Busse) balloon in the Rayleigh–Bénard convection, which contains regions of stable solutions in a space of parameter (Ra, Pr, λ) bounded by various possible instabilities (see Cross and Hobenberg, 1993). In particular, the onset of a $\lambda_\theta \neq 0$ wavelength is similar to the zigzag instability, which is a universal instability associated with low Prandtl number nonlinear convection in weakly confined systems. Experiments in stationary convection show that for the zigzag instability (or for other phase instabilities) the wave vector selection originates from defects (dislocation, grain boundaries etc.) or from finite perturbations using thermal printing (Cross and Hobenberg, 1993), quite similar to our finite perturbations of the axisymmetric solution. The analogous space of parameters in the present system would be (Re, Ro, λ). Thus, the large values of the Rossby number in our flow may be analogous to lower Prandtl number situations in the Rayleigh–Bénard convection.

The characteristics of the computed ring and spiral instabilities are plotted in Figs. 10(a)–(c), together with the experimental, theoretical and numerical results reported in Table 1. The dashed regions correspond to zones, where the flow characteristics vary, e.g., the local value *Re* between the entry and exit sections and also the multiple inclination angles of the spiral in both the experiments and our computations. For the instability results plotted in Fig. 10(a) we find that over the considered *Re* range, the types I and II instabilities are well determined as $\lambda_{\mathrm{I}} \leqslant 12$ and $20 \leqslant \lambda_{\mathrm{II}} \leqslant 30$, respectively. We note that the wavelengths of the three-dimensional instability remain roughly invariant over the range of *Re* considered for the spiral patterns and for the different numbers of spiral arms. For the ring patterns, the wavelength λ_{r} slightly varies with $\bar{r}$ between the entrance and the exit sections. The inclination angle ε displayed in Fig. 10(b) are positive in the range $5° \leqslant \varepsilon_{\mathrm{I}} \leqslant 15°$ for the type I instability and negative in the range $-15° \leqslant \varepsilon_{\mathrm{II}} \leqslant 0°$ for the type II instability. The phase velocities v_ψ (plotted in Fig. 10(c)) shows that the type I instability is well determined by $v_\psi \leqslant 0.1$ (except for the single measurement of Faller and Kaylor, 1966). For the type II instability, v_ψ varies over the range $0.15 \leqslant v_\psi \leqslant 0.60$. We note that our computed results are always well identified in the region of the characteristic parameters, where experiments and theoretical results have located the type II instability. Analysis of the three instability parameters given in Figs. 10(a)–(c) supports our opinion that the present time-dependent solutions indeed correspond to a type II Ekman layer instability.

Recent measurements by Lingwood (1995, 1996) have demonstrated that the type II Ekman layer instability is a convective instability and not an absolute instability. We intend to more precisely analyze this feature in some forthcoming numerical investigations.

Acknowledgements

The authors gratefully acknowledge Professor P. Weidman who carefully read and improved the manuscript, and Professor J.M. Owen and Dr M. Wilson for fruitful discussions. They thank also the editor, Professor B.E. Launder, and the referees for their suggestions. The computations were carried

out on a computer Cray C98, at the CNRS IDRIS Computing Center with support from the Scientific Committee. The AIP Picasso of the Ministère des Affaires Etrangères, the Royal Society – CNRS Cooperative Program, the CNRS-DFG Research Program "Numerical Simulation of Flows" and research contracts involving DGA and SNECMA are also acknowledged. ECA acknowledges financial support from DGICYT (Spain) with grants Nos. PB96-0148 and PB96-0074.

References

Barcilon, V., Pedlosky, J., 1967. On the steady motions produced by a stable stratification in a rapidly rotating fluid. J. Fluid Mech. 29, 673–690.

Bennetts, D.A., Jackson, W.D.N., 1974. Source–sink flows in a rotating annulus: a combined laboratory and numerical study. J. Fluid Mech. 66, 689–705.

Caldwell, D.R., Atta, C.W., 1970. Characteristics of Ekman boundary layer instabilities. J. Fluid Mech. 44, 79–95.

Canuto, C., Hussaini, M.Y., Quarteroni, A., Zang, T.A., 1988. Spectral Methods in Fluids Dynamics. Springer, New York.

Cesaroli, C.P., 1975. Free shear layer instability due to the probes in rotating source–sink flow. J. Fluid Mech. 72, 559–586.

Chew, J.W., Owen, J.M., Pincombe, J.R., 1984. Numerical predictions for laminar source-sink flow in a rotating cylindrical cavity. J. Fluid Mech. 143, 451–466.

Cochran, W.G., 1934. The flow due to a rotating disk. Proc. Cambridge Phil. Soc. 30, 365–375.

Crespo del Arco, E., Maubert, P., Randriamampianina, A., Bontoux, P., 1996. Spatio temporal behaviour in a rotating annulus with a source–sink flow. J. Fluid Mech. 32, 1–27.

Cross M.C., Hohenberg P.C., 1993. Pattern formation outside of equilibrium. Rev. Modern Phys. 65 (3, Part II).

Faller, A.J., 1963. An experimental study of the instability of the laminar Ekman boundary layer. J. Fluid Mech. 15, 560–576.

Faller, A.J., Kaylor, R.E., 1966. Investigations of stability and transition in rotating boundary layers. In: S.I. Pai (Ed.), Dynamics of Fluids and Plasmas, Academic Press, pp. 309–329.

Faller, A.J., 1991. Instability and transition of the disturbed flow over a rotating disc. J. Fluid Mech. 230, 245–269.

Fowlis, W.W., Hide, R., 1965. Thermal convection in a rotating annulus of liquid: effect of viscosity on the transition between axisymmetric and non-axisymmetric flow regimes. J. Atmos. Sci. 22, 541–558.

Gauthier, P., Gondret, P., Rabaud, M., 1999. Axisymmetric propagating vortices in the flow between a stationary and a rotating disk enclosed by a cylinder. J. Fluid Mech. 386, 105–127.

Goda, K., 1979. A multistep technique with implicit difference schemes for calculating two and three-dimensional cavity flows. J. Comp. Phys. 30, 76–95.

Gottlieb, D., Orszag, S.A., 1977. Numerical Analysis of Spectral Methods: Theory and Application. SIAM, PA, USA.

Gresho, P., Sani, R.L., 1987. On pressure boundary conditions for the incompresible Navier–Stokes equations. Int. J. Numer. Meth. Fluids 7, 137.

Greenspan, H.P., 1969. The Theory of Rotating Fluids. Cambridge University Press, Cambridge.

Haldenwang, P., Labrosse, G., Abboudi, S., Deville, M., 1984. Chebyshev 3D spectral and 2D pseudo-spectral solvers for the Helmholtz equation. J. Comput. Phys. 55, 115–128.

Hide, R., 1968. On source–sink flows stratified in a rotating annulus. J. Fluid Mech. 32, 737–764.

Hignett, P., White, A.A., Carter, R.D., Jackson, W.D.N., Small, R.M., 1985. A comparison of laboratory measurements and numerical simulations of baroclinic wave flows in a rotating cylindrical annulus. Quart J. R. Met. Soc. 111, 131–154.

Hopfinger, C.E., Linden, P.F., 1990. The effect of background rotation in fluid motion: a report on Euromech. J. Fluid Mech. 211, 417–435.

Hugues, S., Serre, E., Crespo del Arco, E., Randriamampianina, A., Bontoux, P., 1998. Instabilité tridimensionnelle de la couche d'Ekman dans une configuration annulaire avec flux forcé. C.R. Acad. Sci. Paris 326, Série IIb, 873–879.

Hugues, S. 1998. Développement d'un algorithme de projection pour méthodes psudo-spectrales: application à la simulation d'instabilités tridimensionnelles dans les cavités tournantes. Modélisation d'écoulements turbulents dans les systèmes rotor–stator. Ph.D. thesis, Université de la Méditerranée, Marseille.

Hugues, S., Randriamampianina, A., 1998. An improved projection scheme applied to pseudo-spectral methods for the incompressible Navier–Stokes equations. Int. J. Numer. Meth. Fluids 28, 501–521.

Lilly, D.K., 1966. On the instability of Ekman boundary flow. J. Atmos. Sci. 23, 481–490.

Lingwood, R.J., 1995. Absolute instability of the boundary layer on a rotating disk. J. Fluid Mech. 299, 17–33.

Lingwood, R.J., 1996. An experimental study of absolute instability of the rotating-disk boundary-layer flow. J. Fluid Mech. 314, 373–405.

Marlatt, S.W., Biringen, S., 1995. Numerical simulation of spatially evolving Ekman layer instability. Phys. Fluids 7, 449–451.

Owen, J.M., Pincombe, J.R., 1980. Velocity measurements inside a rotating cavity with a radial outflow of fluid. J. Fluid Mech. 99, 111–127.

Owen, J.M., Pincombe, J.R., Rogers, R.H., 1985. Source–sink flow inside a rotating cylindrical cavity. J. Fluid Mech. 155, 233–265.

Owen, J.M., Rogers, R.H., 1989. Heat transfer in rotating disk systems. In: Morris, W.D. (Ed.), Rotor–Stator Systems, vol. 1. RSP, Wiley, New York.

Owen, J.M., Rogers, R.H., 1995. Heat transfer in rotating disk systems. In: Morris, W.D. (Ed.), Rotating Cavities, vol. 2. RSP, Wiley, New York.

Raspo, I., 1996. Méthodes spectrales et de décomposition de domaine pour les ecoulements complexes confinés en rotation. Ph.D. thesis, Université de la Méditerranée, Marseille.

Rothman, E., 1991. Reducing round-off error in Chebyshev pseudo-spectral computations. In: Durand, M., El Dabaghi, F. (Eds.), High Performance Computing II. North Holland, Amsterdam, p. 423.

Savas, O., 1987. Stability of Bödewadt flow. J. Fluid Mech. 183, 77–94.

Schouveiler, L., Gal, P., Chauve, M.P., Takeda, Y., 1999. Spiral and Circular waves in the flow between a rotating and a stationary disk. Experiments in Fluids 26, 179–187.

Serre, E., Crespo del Arco, E., Bontoux, P., 1999a. Instabilité tridimensionnelle dans une cavité de type rotor-stator. C.R. Acad. Sci. Paris, Série IIb 327, 1139–1146.

Serre, E., Crespo del Arco, E., Bontoux, P., 1999b. Annular and spiral patterns in a flow between a rotating and a stationary disk. J. Fluid Mech. (under revision) .

Serre, E., Pulicani, J.P., 2000. A 3D pseudo-spectral method for convection in a rotating cylinder. Comput. Fluids (in press).

Tatro, P.R., Mollö-Christensen, E.L., 1967. Experiments on Ekman layer instability. J. Fluid Mech. 28, 531–543.

Vanel, J.M., Peyret, R., Bontoux, P., 1986. A pseudo-spectral solution of vorticity-streamfunction equations using the influence matrix technique. In: Morton, K.W., Baines, M.J., (Eds.), Numerical Methods of Fluid Dynamics II. pp. 463–475.

Von Karman, T., 1921. Über laminare und turbulente Reibung. Z. Angew. Mech. 1, 233–252.

Weidman, P.D., 1976. On the spin-up and spin-down of a rotating fluid. Part 2: Measurements and stability. J. Fluid Mech. 77 (4), 709–735.

Wilkinson, S.P., Malik, M.R., 1987. Stability experiments in the flow over a rotating disk. AIAA J. 23 (4), 588–595.